Featured in Physics

Quantifying Spin-Mixed States in Ferromagnets

Justin M. Shaw, Ronny Knut, Abigail Armstrong, Sumanta Bhandary, Yaroslav Kvashnin, Danny Thonig, Erna K. Delczeg-Czirjak, Olof Karis, T. J. Silva, Eugen Weschke, Hans T. Nembach, Olle Eriksson, and Dario A. Arena

¹Quantum Electromagnetics Division, National Institute of Standards and Technology, Boulder, Colorado 80305, USA

²Department of Physics and Astronomy, University Uppsala, S-75120 Uppsala, Sweden

³Department of Physics, University of South Florida, Tampa, Florida 33620, USA

⁴School of Physics and CRANN Institute, Trinity College Dublin, The University of Dublin, Dublin 2, Ireland

⁵School of Science and Technology, Örebro University, SE-701 82 Örebro, Sweden

⁶Helmholtz-Zentrum Berlin für Materialien und Energie, Wilhelm-Conrad-Röntgen-Campus BESSY II, D-12489 Berlin, Germany

⁷Department of Physics, University of Colorado, Boulder, Colorado 80309, USA

(Received 19 May 2021; accepted 8 September 2021; published 8 November 2021)

We quantify the presence of spin-mixed states in ferromagnetic 3D transition metals by precise measurement of the orbital moment. While central to phenomena such as Elliot-Yafet scattering, quantification of the spin-mixing parameter has hitherto been confined to theoretical calculations. We demonstrate that this information is also available by experimental means. Comparison of ferromagnetic resonance spectroscopy with x-ray magnetic circular dichroism results show that Kittel's original derivation of the spectroscopic g factor requires modification, to include spin mixing of valence band states. Our results are supported by ab initio relativistic electronic structure theory.

DOI: 10.1103/PhysRevLett.127.207201

Spin-orbit coupling (SOC) in ferromagnets enables many mechanisms that affect the efficiency and performance of many magnetic phenomena [1], e.g., functionality of spintronic devices, Dzyaloshinskii-Moriya interaction and topological magnetism [2-4], magnetocrystalline anisotropy [5], magneto-optic and magnetic dichroism [6], as well as quantum spin-Hall effect [7]. On a microscopic band structure level, SOC affects the purity of spinpolarized bands in a magnetic metal—essentially mixing the spin states [8]. Such spin-mixing effects can lead to Elliot-Yafet spin scattering which drives the relaxation of magnetization dynamics [8-12]. Although assumed, the absence of measurement capability to quantify spin mixing leads to additional uncertainty of the role such scattering mechanisms play in, for example, ultrafast magnetization dynamics and switching [9]. SOC also generates finite orbital moments in solids that would otherwise be entirely quenched from the crystal field [13]. Quantifying the orbital moment in thin films is primarily limited to ferromagnetic resonance spectroscopy (FMR) and x-ray spectroscopic methods such as magnetic circular dichroism (XMCD) because neutron scattering approaches [14–16] and electron magnetic circular dichroism [17] lack a sufficient signal-to-noise ratio needed for the precise measurement of orbital moments in thin films.

In the case of FMR, the orbital moment is determined through the measurement of the spectroscopic g factor. The fundamental assumption that defines g is that the FMR frequency ω is proportional to the effective field $H_{\rm eff}$ given

by the so-called Kittel equation [18] $\hbar\omega = g\mu_B\mu_0H_{\rm eff}$, where \hbar is the reduced Planck's constant, μ_0 is the permeability of free space, and μ_B is the Bohr magneton. Using first-order perturbation theory, Kittel was able to relate g to the ratio of orbital moment μ_L and spin moment μ_S [13,19],

$$\frac{\mu_L}{\mu_S} = \frac{g-2}{2} \ . \tag{1}$$

Originally derived in 1949 by Kittel, this expression has been used and applied in almost all FMR based experiments used to characterize ferromagnetic systems. In its derivation, Kittel intentionally dismisses second-order terms that take into account spin-mixed states. Although acknowledged, they were assumed to be insignificant within the measurement limitations of the time. However, modern broadband FMR techniques can routinely measure values of g with a precision that goes to the third decimal place or approximately 0.1% of the g factor [20,21]. As a consequence, this assumption must be reexamined.

Core-level x-ray spectroscopy can also be used to determine μ_L and μ_S . Such element-specific measurements are typically collected at synchrotron-based light sources [22–25], and more recently, tabletop light sources [26–28]. The absorption of circularly polarized x-ray photons resonant with core-level energies excites electrons with predominantly opposite spins across the spin-orbit split L_3 and L_2 edges of 3D transition metals and an imbalance of

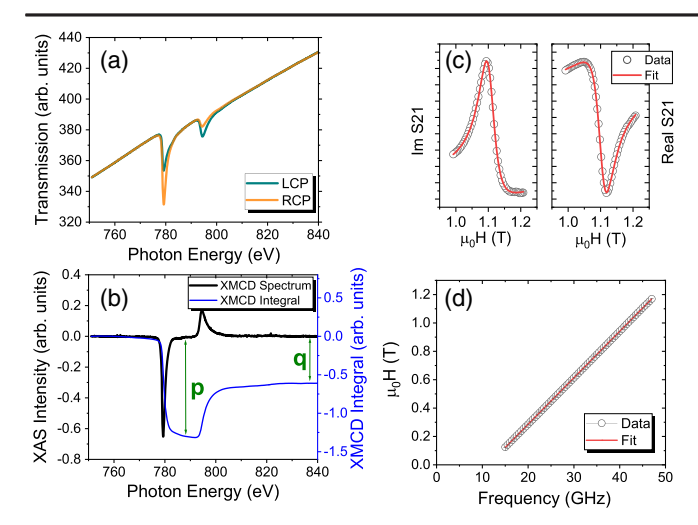


FIG. 1. (a) Transmission spectra across the Co L edge for both left hand circular polarized (LCP) and right hand circular polarized (RCP) photons for the $t_{\rm CoFe}=0.26$ nm sample. (b) The normalized XMCD spectrum taken from the data in (a) along with the integral of the XMCD spectrum. Graphic representations of p and q are indicated. (c) Example of the imaginary and real S21 signal measured as the magnetic field is swept through the FMR at 45 GHz. (d) The resonance field $H_{\rm res}$ versus frequency along with the fit used to determine the g factor for the $t_{\rm CoFe}=0.22$ nm sample.

up and down spin final states in the unoccupied conduction band produces a large asymmetry in the absorption probability. An example of this effect for the Co L edge is given in Fig 1(a). The separate contributions of μ_L and μ_S can be determined by applying appropriate magneto-optical sum rules that are essentially weighted sums of the dichroic spectrum normalized by the spin-integrated x-ray absorption spectrum. The ratio of the orbital and effective spin moments simplifies to [22,29–33],

$$\frac{\mu_L}{\mu_S^{\rm eff}} = -\left(\frac{2}{3}\right) \frac{q}{3p - 2q} \;, \tag{2} \label{eq:2}$$

where q is the value of the XMCD spectrum integrated across both the L_3 and L_2 edges, p is the value of the XMCD integral across only the L_3 edge; we refer to Fig. 1(b) for an illustration.

In this Letter, we compare values of μ_L/μ_S obtained with both XMCD and FMR taken on identical samples. We account for all known factors that can lead to a discrepancy between measurement approaches and show that higher-order corrections that take into account the mixed spin states must be included in Eq. (1). More importantly, this analysis leads to the ability to quantify the spin-mixing parameter for valence electron states. The measurements agree with results from relativistic electronic structure theory.

Samples were dc magnetron sputter deposited while being rotated at ambient temperature in a chamber with a base pressure of approximately 1.3×10^{-7} Pa $(1 \times 10^{-9} \text{ Torr})$.

The sample multilayer structure consisted of eight bilayers of $[Co_{90}Fe_{10}(t_{CoFe})/Ni(3t_{CoFe})]$ with an additional $Co_{90}Fe_{10}(t_{CoFe})$ layer at the top interface. A Ta(3)/Cu(5) seed layer and a Cu(3)/Ta(3) capping layer were also used, where the thickness is given in nanometers. Samples were deposited simultaneously on rigid, thermally oxidized Si substrates and Si_3N_4 membranes. Both substrates produce identical samples, as confirmed by FMR measurements taken on both substrates. Additional details of sample fabrication and characterization can be found in Ref. [34]. A 20 nm thick $Ni_{80}Fe_{20}$ sample was also fabricated from a stoichiometric sputtering target.

The magnetic anisotropy and g were characterized with broadband vector network analyzer (VNA) based FMR in the perpendicular geometry. After the sample was placed face down on the waveguide, the complex transmission parameter S21 was measured using a VNA with a bandwidth of 1–70 GHz. Figure 1(c) shows an example of the real and imaginary S21 measured at a fixed frequency as the magnetic field is swept through the FMR. These data are analyzed via the methods outlined in Ref. [35]. The resonance field as a function of frequency is fit to the out-of-plane Kittel equation for a thin film as given as $f(H_{\rm res}) = g\mu_0\mu_B/2\pi\hbar(H_{\rm res}-M_{\rm eff})$ where $M_{\rm eff}$ is the effective magnetization defined as $M_{\text{eff}} = M_s - H_k$, where M_s is the saturation magnetization and H_k is the perpendicular magnetic anisotropy. An example data set that is fit is shown in Fig. 1(d). Since the in-plane anisotropy is negligible in our case (<1 mT), such a term is not included. We apply the methods presented in Ref. [20] to increase the precision of g. It is important to point out that this method for determining g is independent of assumptions made about inclusion or exclusion of additional anisotropy terms as well as any misalignment of the external magnetic field during the measurement [20,21].

In XMCD spectroscopy, the magnetic signal is proportional to the projection of the photon helicity vector along the magnetization direction of the sample $(\vec{c}_{h\nu}\cdot\vec{m})$. The dichroic spectrum is typically generated by reversing either the direction of the helicity or the magnetization, and recording the difference in the x-ray absorption intensity. We employ both methods in separate studies of $\text{Co}_{90}\text{Fe}_{10}/\text{Ni}$ multilayers and $\text{Ni}_{80}\text{Fe}_{20}$ thin films.

For the $\mathrm{Co_{90}Fe_{10}}/\mathrm{Ni}$ multilayers, we employed the soft x-ray elliptical undulator at BESSY II to perform transmission x-ray absorption spectroscopy (XAS) and XMCD measurements. A superconducting magnet was used to apply a saturating static magnetic field of $\mu_0 H = 3$ T oriented both along the photon beam direction and perpendicular to the plane of the sample. The photon energy was scanned through the transition L edge for Fe, Co, and Ni, which spans 695–760 eV, 750–840 eV, and 820–920 eV, respectively. The 90% circular polarization of the soft x-rays was adjusted between left- and right-polarization states by the undulator. All XAS data were

corrected for the spectral contribution of the nonmagnetic Ta(3)/Cu(8)/Ta(3) layers in each sample following the procedure in Ref. [32], and the resulting transmission spectra were converted to absorption spectra via Beer's law. The normalization process yielded nearly identical preedge and postedge backgrounds. The difference in the background was less than 0.1% for Co and Ni and 1% for Fe; we attribute the increased background variation in the Fe spectra to the low concentration of Fe in the ML samples. These small background differences were used to correct the XAS spectra to ensure the integrated XMCD spectra (see below) exhibited flat preedge and postedge spectral regions suitable for sum rules analyses.

We also acquired XMCD spectra for a 20 nm thin film of $Ni_{80}Fe_{20}$, measured at beam line U4B of the VUV ring at the National Synchrotron Light Source at Brookhaven National Lab. Here, the degree of circular polarization was 70% and the film was saturated in the out-of-plane direction in a ± 1.5 T field. XMCD spectra were acquired by toggling the direction of the magnetic field for each photon energy.

Figure 2(a) shows the elemental values of $\mu_L/\mu_S^{\rm eff}$ obtained from XMCD measurements of the ML samples for Fe, Co, and Ni, respectively. All values of $\mu_L/\mu_S^{\rm eff}$ show a gradual and small increase at higher values of $1/t_{\rm CoFe}$, consistent with an expected linear dependence on $1/t_{\rm CoFe}$ [34,36,37]. The larger scatter and error bars for Fe are a result of the reduced SNR and large background signal owing to the small concentration of Fe relative to Co and Ni. To directly compare to the FMR results, we must

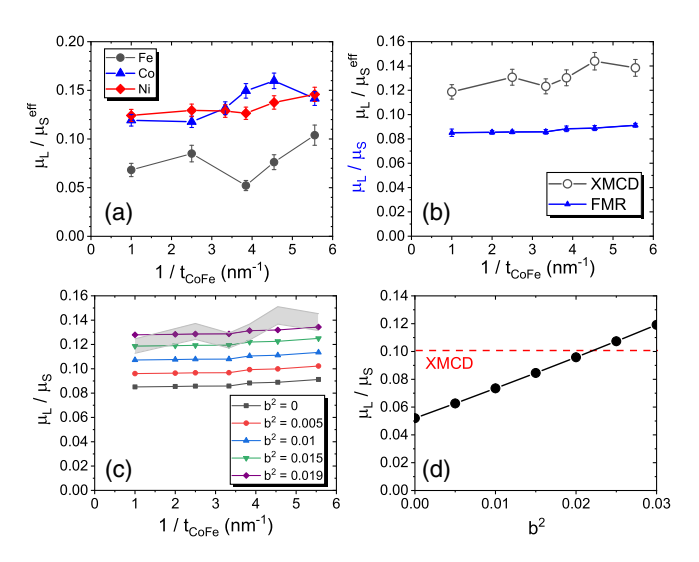


FIG. 2. (a) Elemental values of $\mu_L/\mu_S^{\rm eff}$ as a function of $1/t_{\rm CoFe}$ for the ML samples. (b) Comparison of the total value of $\mu_L/\mu_S^{\rm eff}$ from XMCD and μ_L/μ_S from FMR. (c) Values of μ_L/μ_S for different values of b^2 . The shaded regions is XMCD result bounded by the error bars. (d) values of μ_L/μ_S versus b^2 for the Ni₈₀Fe₂₀ sample. The value obtained from XMCD is indicated as the horizontal dashed line.

calculate the total of $\mu_L/\mu_S^{\rm eff}$ over all the constituents in our sample, weighing elemental values to both the spin moment and the fractional atomic concentration (see Supplemental Material (SM) [38]). Figure 2(b) is plot of μ_L/μ_S and $\mu_L/\mu_S^{\rm eff}$ as a function of the inverse thickness as determined via FMR and XMCD, respectively. These data show that XMCD yields larger values relative to FMR by approximately 50%, which is well outside of the error bars of each measurement.

One factor that may contribute to an uncertainty in the XMCD results is the effect of the spin dipole operator T_z to the XMCD signal [39]. It is for this reason that Eq. (2) has an effective spin moment in the denominator, which is related to the spin moment μ_S via $\mu_S^{\text{eff}} = \mu_S - 7 \langle T_z \rangle \mu_B / \hbar$. Previous calculations of $\langle T_z \rangle$ for Fe, Co, and Ni indicate it is at most a few percent of the spin moment [33]. However, those same calculations also show that the spin dipole moment can be as high as 12% of the spin moment at surfaces and interfaces in some materials. Furthermore, measurements taken on ultrathin epitaxial Co layers sandwiched between Au indicate the dipole term can be as high as $-0.86 \mu_B$ or approximately 50% of the spin moment in the single monolayer limit [40]. To address this matter, we performed explicit ab initio calculations of the spin dipole moment of our sample geometries (see SM [38] and Refs. [41-46] for details). Our calculations show a maximum enhancement of the $7\langle T_z \rangle$ value as high as 3.6% in Co and 6.7% in Ni at 3 monolayers in thickness. However, extending the calculation to values of thickness used in this study, the value of $7\langle T_z \rangle$ becomes at most a few percent in Co and is negligible for Ni for most samples in this study. This is consistent with previous calculations and experimental determination of $\langle T_z \rangle$ in similar Co/Ni multilayers [36,37]. As a result, effects of $\langle T_z \rangle$ cannot explain the discrepancy between XMCD and FMR.

We argue here that the discrepancy between FMR and XMCD results originate from Kittel's original derivation of g [18]. In the original derivation of Eq. (1), only first order of b (spin-mixed states), were considered, where b is defined by the spin-up wave function $|\Psi^{\uparrow}\rangle = a|\uparrow\rangle + b|\downarrow\rangle$ and spin-down wave function $|\Psi^{\downarrow}\rangle = a|\downarrow\rangle + b|\uparrow\rangle$ and $a^2 + b^2 = 1$ (see SM [38] and Ref. [47] for more information). However, the increased precision of modern broadband FMR may lead to the possibility of observing higher-order effects of b. Following Kittel's original derivation, a simple inclusion of second-order terms in b (see SM [38] for full derivation) yields the following relation between g and μ_L/μ_S ,

$$\left(\frac{\mu_L}{\mu_S}\right)_{\text{EMP}} = \frac{g - 2 + 4\langle b^2 \rangle}{2(1 - 2\langle b^2 \rangle)},\tag{3}$$

where $\langle b^2 \rangle$ is the spin-mixing parameter with the assumption that $\langle b^2 \rangle \ll 1$. By comparison with Eq. (1), this shows that including the effects of spin mixing reduces the value of the measured g factor. This can lead to an underestimation of

 μ_L/μ_S if $\langle b^2 \rangle$ is neglected. We quantitatively explore the effect of the second-order term on our data by replotting $(\mu_L/\mu_S)_{\rm FMR}$ for various values of $\langle b^2 \rangle$ that range from 0 to 0.019 in Fig. 2(c). We see that exceptionally small values of $\langle b^2 \rangle$ can yield significant changes in $(\mu_L/\mu_S)_{\rm FMR}$. A fit between the XMCD and FMR data yield a value of $\langle b^2 \rangle = 0.019 \pm 0.001$, which is visually represented in Fig. 2(c).

Similar conclusions are also obtained from a 20 nm thick $N_{80}\mathrm{Fe}_{20}$ film. Application of the sum rules to the XMCD data yields values of $(\mu_L/\mu_S)_{\mathrm{Ni}}=0.1304\pm0.006$ and $(\mu_L/\mu_S)_{\mathrm{Fe}}=0.0668\pm0.005$ for the Ni and Fe and a total value of $(\mu_L/\mu_S)_{\mathrm{total}}=0.0998\pm0.006$. Precision FMR measurements taken in the perpendicular geometry on an identical 20 nm $\mathrm{Ni}_{80}\mathrm{Fe}_{20}$ sample yields a value of $g=2.104\pm0.002$ and an uncorrected ratio $(\mu_L/\mu_S)_{\mathrm{FMR}}=0.052\pm0.001$. To visualize the effect of a finite $\langle b^2 \rangle$, we plot $(\mu_L/\mu_S)_{\mathrm{FMR}}$ determined from Eq. (3) as a function of the spin-mixing parameter $\langle b^2 \rangle$ in Fig. 2(d). Also included as the horizontal dashed line is the value obtained from XMCD. A fit yields a value of $\langle b^2 \rangle = 0.022\pm0.003$.

For comparison, we present ab initio calculations of the value of $\langle b^2 \rangle$. The first-principles density functional theory (DFT) calculations are performed with the Vienna ab initio simulation package [48]. Plane-wave projector augmented wave basis is used in Perdew-Burke-Ernzerhof generalized gradient approximation for exchange-correlation potential. The energy cutoff used is 400 eV. The Ni/Co multilayer consists of 3 Co layers and 6 Ni layers, cleaved along the (fcc)111 direction. To facilitate the Ni-Co interface reconstruction, we have optimized the atomic positions in the multilayer by minimizing the Hellman-Feynman force up to 0.1 eV/nm. The calculations of the spin-mixing parameter $\langle b^2 \rangle$ are converged with respect to the k-mesh sampling in the Brillouin zone. Furthermore, our DFT calculations are complemented by Slater-Koster parametrized tight binding (TB) calculations with Cahmd [49]. These results are summarized in Table I for bcc Fe, fcc Co, and fcc Ni, together with data for an Co/Ni multilayer with the same geometry, structure, and lattice constants as studied experimentally here. We also include previous calculations for Fe, Co, and Ni. One may note that all theoretical calculations show some scatter in the detailed values of $\langle b^2 \rangle$, but that they all give the same order of magnitude.

Both samples studied here have 75 to 80 at.% Ni content and therefore it is no surprise the we obtain similar values

TABLE I. Calculated values of $\langle b^2 \rangle$ at RT (25 meV) or *80 meV.

	Fe	Co	Ni	Co/Ni
This work (DFT)	0.045	0.030	0.033	0.051
This work (TB)	0.031	0.012	0.024	0.027
Refs. [9,12]	0.024	0.011	0.025	
Ref. [8]	0.028*		0.025*	

for $\langle b^2 \rangle$. Future work is required to make more comparisons between XMCD and FMR that span materials having varying degrees of spin mixing. Since Ref. [50] makes use of the same FMR protocols, we make a crude comparison between elemental films of Fe and Ni and other published results from XMCD. However, since the sample structure, thickness, and growth conditions differ, quantitative analysis is not possible. In addition, transmission XMCD is the only method that can give absolute absorption cross sections, so detection schemes used in previous studies may introduce additional artifacts [33]. For Ni, FMR yields $g=2.184\pm0.002$ and an uncorrected $\mu_L/\mu_S = 0.095$, while XMCD yields $\mu_L/\mu_S = 0.25$ [51], 0.28 [31], and 0.19 [30]. The large discrepancy between FMR and XMCD in Ni supports our findings. Similarly for Fe, FMR yields a value of $q = 2.085 \pm 0.003$ and an uncorrected $\mu_L/\mu_S = 0.042$, whereas published values obtained with XMCD yield $\mu_L/\mu_S = 0.055$ [52], 0.043 [32], and 0.058 [53]. Here the difference between FMR and XMCD is still present, but more subtle, suggesting a reduced spin-mixing parameter for Fe.

While identifying the need for higher-order terms in Kittel's original derivation is a substantial finding in and of itself, the significance of this work is better expressed in gaining the ability to experimentally measure the parameter $\langle b^2 \rangle$. Further refinement of Eq. (3) though a more rigorous second-order perturbation theory may lead to even more accurate determination of $\langle b^2 \rangle$. Prior to this, values of $\langle b^2 \rangle$ could be determined only through first-principles calculations, which are challenging due to the required numerical accuracy. The $\langle b^2 \rangle$ values are very sensitive and often require significantly large k-mesh sampling of the Brillouin zone which makes the calculations numerically expensive. Moreover, a slight variation in the evaluated $\langle b^2 \rangle$ values is to be expected within different DFT based techniques owing to the smallness of the parameter, and the sensitivity with respect to computational parameters such as choice of basis set, treatment of relativity, dependence on energy function, etc. Experimental evidence of the spin-mixing parameter was primarily limited to the Elliott-Yafet description of spin scattering that is often used to explain ultrafast magnetization dynamics [8–11]. However, quantification of $\langle b^2 \rangle$ with ultrafast experiments is highly dependent on the model used to fit such data [9]. Such complex models are continuously evolving since they include many interactions between spins, photons, phonons, magnons, and spin currents [9,54–56]. By independently quantifying $\langle b^2 \rangle$ through the quantification of orbital moments, such ultrafast models (or more generally Elliott-Yafet spin scattering) can be refined by excluding $\langle b^2 \rangle$ as a fitting parameter. Most importantly, quantifying the ground state spin-mixing parameter has profound implications for any condensed matter system where spin plays an important role in the overall Hamiltonian where the description of "pure" spin states is not accurate: such as ferrimagnets,

antiferromagnets, Weyl semimetals, superconductors, and topological insulators.

The authors are grateful to Mark Stiles for providing valuable feedback and comments to our manuscript and analysis. J. M. S., H. T. N., and T. J. S. acknowledge support from U.S. Department of Energy Office of Basic Energy Sciences Grant No. DE-SC0017643. D. A. A. acknowledges support from the National Science Foundation under Grant No. ECCS-1952957 and the University of South Florida Nexus Initiative (UNI) Award. S. B. acknowledges support from Science Foundation Ireland (19/EPSRC/3605) and the Engineering and Physical Sciences Research Council (EP/ S030263/1). O. E. acknowledges support from eSSENCE, STandUPP, SNIC, the Swedish Research Council (VR) under Contracts No. 2019-03569, No. 2019-03666, No. 2013-08316, and No. 2016-04524, the foundation for strategic research, the Swedish Energy Agency, Knut and Alice Wallenberg Foundation, and the ERC (synergy grant FASTCORR, Project No. 854843). Use of the National Synchrotron Light Source, Brookhaven National Laboratory was supported by the U.S. Department of Energy, Office of Science, Office of Basic Energy Sciences, under Contract No. DE-AC02-98CH10886. Some measurements were carried out at the High-Field Diffractometer at UE46-PGM1 end station at BESSY II at Helmholtz-Zentrum Berlin.

- [1] A. Soumyanarayanan, N. Reyren, A. Fert, and C. Panagopoulos, Nature (London) **539**, 509 (2016).
- [2] I. Dzyaloshinsky, J. Phys. Chem. Solids 4, 241 (1958).
- [3] T. Moriya, Phys. Rev. 120, 91 (1960).
- [4] M. Bode, M. Heide, K. von Bergmann, P. Ferriani, S. Heinze, G. Bihlmayer, A. Kubetzka, O. Pietzsch, S. Blügel, and R. Wiesendanger, Nature (London) 447, 190 (2007).
- [5] P. Bruno, Phys. Rev. B 39, 865 (1989).
- [6] J. L. Erskine and E. A. Stern, Phys. Rev. B 8, 1239 (1973).
- [7] B. A. Bernevig and S.-C. Zhang, Phys. Rev. Lett. 96, 106802 (2006).
- [8] M. Haag, C. Illg, and M. Fähnle, Phys. Rev. B 90, 134410 (2014).
- [9] B. Koopmans, G. Malinowski, F. D. Longa, D. Steiauf, M. Fähnle, T. Roth, M. Cinchetti, and M. Aeschlimann, Nat. Mater. 9, 259 (2010).
- [10] R. J. Elliott, Phys. Rev. 96, 266 (1954).
- [11] K. Carva, M. Battiato, and P. M. Oppeneer, Phys. Rev. Lett. 107, 207201 (2011).
- [12] D. Steiauf and M. Fähnle, Phys. Rev. B **79**, 140401(R) (2009).
- [13] J. H. Van Vleck, Phys. Rev. 78, 266 (1950).
- [14] A. Schreyer, T. Schmitte, R. Siebrecht, P. Bödeker, H. Zabel, S. H. Lee, R. W. Erwin, C. F. Majkrzak, J. Kwo, and M. Hong, J. Appl. Phys. 87, 5443 (2000).
- [15] M. R. Fitzsimmons, S. D. Bader, J. A. Borchers, G. P. Felcher, J. K. Furdyna, A. Hoffmann, J. B. Kortright, I. K. Schuller, T. C. Schulthess, S. K. Sinha, M. F. Toney, D. Weller, and S. Wolf, J. Magn. Magn. Mater. 271, 103 (2004).

- [16] C. J. Thompson, D. Reig-i-Plessis, L. Kish, A. A. Aczel, B. Zhang, E. Karapetrova, G. J. MacDougall, and C. Beekman, Phys. Rev. Mater. 2, 104411 (2018).
- [17] P. Schattschneider, S. Rubino, C. Hébert, J. Rusz, J. Kuneš, P. Novák, E. Carlino, M. Fabrizioli, G. Panaccione, and G. Rossi, Nature (London) 441, 486 (2006).
- [18] C. Kittel, Phys. Rev. 76, 743 (1949).
- [19] A. J. P. Meyer and G. Asch, J. Appl. Phys. **32**, S330 (1961).
- [20] J. M. Shaw, H. T. Nembach, T. J. Silva, and C. T. Boone, J. Appl. Phys. 114, 243906 (2013).
- [21] C. Gonzalez-Fuentes, R. K. Dumas, and C. García, J. Appl. Phys. **123**, 023901 (2018).
- [22] J. Stöhr, J. Magn. Magn. Mater. 200, 470 (1999).
- [23] W. Kuch, in *Magnetism: A Synchrotron Radiation Approach*, edited by E. Beaurepaire, H. Bulou, F. Scheurer, and J.-P. Kappler (Springer, Berlin, Heidelberg, 2006), pp. 275–320.
- [24] F. Macià, P. Warnicke, D. Bedau, M.-Y. Im, P. Fischer, D. A. Arena, and A. D. Kent, J. Magn. Magn. Mater. 324, 3629 (2012).
- [25] J. A. Moyer, C. A. F. Vaz, D. P. Kumah, D. A. Arena, and V. E. Henrich, Phys. Rev. B 86, 174404 (2012).
- [26] S. Kneip, C. McGuffey, J. L. Martins, S. F. Martins, C. Bellei, V. Chvykov, F. Dollar, R. Fonseca, C. Huntington, G. Kalintchenko, A. Maksimchuk, S. P. D. Mangles, T. Matsuoka, S. R. Nagel, C. a. J. Palmer, J. Schreiber, K. T. Phuoc, A. G. R. Thomas, V. Yanovsky, L. O. Silva, K. Krushelnick, and Z. Najmudin, Nat. Phys. 6, 980 (2010).
- [27] T. Popmintchev, M.-C. Chen, P. Arpin, M. M. Murnane, and H. C. Kapteyn, Nat. Photonics 4, 822 (2010).
- [28] O. Kfir, P. Grychtol, E. Turgut, R. Knut, D. Zusin, D. Popmintchev, T. Popmintchev, H. Nembach, J. M. Shaw, A. Fleischer, H. Kapteyn, M. Murnane, and O. Cohen, Nat. Photonics **9**, 99 (2015).
- [29] B. T. Thole, P. Carra, F. Sette, and G. van der Laan, Phys. Rev. Lett. 68, 1943 (1992).
- [30] P. Carra, B. T. Thole, M. Altarelli, and X. Wang, Phys. Rev. Lett. 70, 694 (1993).
- [31] W. L. O'Brien and B. P. Tonner, Phys. Rev. B 50, 12672 (1994).
- [32] C. T. Chen, Y. U. Idzerda, H.-J. Lin, N. V. Smith, G. Meigs, E. Chaban, G. H. Ho, E. Pellegrin, and F. Sette, Phys. Rev. Lett. **75**, 152 (1995).
- [33] G. van der Laan and A. I. Figueroa, Coord. Chem. Rev. 277–278, 95 (2014).
- [34] J. M. Shaw, H. T. Nembach, and T. J. Silva, Phys. Rev. B 87, 054416 (2013).
- [35] H. T. Nembach, T. J. Silva, J. M. Shaw, M. L. Schneider, M. J. Carey, S. Maat, and J. R. Childress, Phys. Rev. B 84, 054424 (2011).
- [36] S. Andrieu, T. Hauet, M. Gottwald, A. Rajanikanth, L. Calmels, A. M. Bataille, F. Montaigne, S. Mangin, E. Otero, P. Ohresser, P. Le Fèvre, F. Bertran, A. Resta, A. Vlad, A. Coati, and Y. Garreau, Phys. Rev. Mater. 2, 064410 (2018).
- [37] M. Gottwald, S. Andrieu, F. Gimbert, E. Shipton, L. Calmels, C. Magen, E. Snoeck, M. Liberati, T. Hauet, E. Arenholz, S. Mangin, and E. E. Fullerton, Phys. Rev. B 86, 014425 (2012).
- [38] See Supplemental Material at http://link.aps.org/ supplemental/10.1103/PhysRevLett.127.207201 for the detailed calculation of the g-factor that includes spin-mixed

- valence states, calculation of the total orbital to spin ratio, calculation of the spin-dipole moment, estimation of the XMCD error, and additional examples of XMCD and FMR data.
- [39] G. van der Laan, J. Phys. Condens. Matter 10, 3239 (1998).
- [40] D. Weller, J. Stöhr, R. Nakajima, A. Carl, M. G. Samant, C. Chappert, R. Mégy, P. Beauvillain, P. Veillet, and G. A. Held, Phys. Rev. Lett. 75, 3752 (1995).
- [41] O. Šipr, J. Minár, and H. Ebert, Europhys. Lett. 87, 67007 (2009).
- [42] S. Bhandary, S. Ghosh, H. Herper, H. Wende, O. Eriksson, and B. Sanyal, Phys. Rev. Lett. 107, 257202 (2011).
- [43] S. Stepanow, A. Mugarza, G. Ceballos, P. Moras, J. C. Cezar, C. Carbone, and P. Gambardella, Phys. Rev. B 82, 014405 (2010).
- [44] R. Wu and A. J. Freeman, Phys. Rev. Lett. 73, 1994 (1994).
- [45] J. Stöhr and H. König, Phys. Rev. Lett. 75, 3748 (1995).
- [46] T. Oguchi and T. Shishidou, Phys. Rev. B 70, 024412 (2004).
- [47] M. Blume, S. Geschwind, and Y. Yafet, Phys. Rev. 181, 478 (1969).
- [48] G. Kresse and J. Furthmüller, Phys. Rev. B 54, 11169 (1996).

- [49] D. Thonig, https://Cahmd.Gitlab.Io/Cahmdweb/ (2013).
- [50] M. A. W. Schoen, J. Lucassen, H. T. Nembach, T. J. Silva, B. Koopmans, C. H. Back, and J. M. Shaw, Phys. Rev. B 95, 134410 (2017).
- [51] S. S. Dhesi, H. A. Dürr, G. van der Laan, E. Dudzik, and N. B. Brookes, Phys. Rev. B 60, 12852 (1999).
- [52] Y. Guan, C. Scheck, and W. E. Bailey, J. Magn. Magn. Mater. 321, 1039 (2009).
- [53] Y. B. Xu, M. Tselepi, E. Dudzik, C. M. Guertler, C. A. F. Vaz, G. Wastlbauer, D. J. Freeland, J. A. C. Bland, and G. van der Laan, J. Magn. Magn. Mater. 226–230, 1643 (2001).
- [54] M. Battiato, K. Carva, and P. M. Oppeneer, Phys. Rev. Lett. 105, 027203 (2010).
- [55] E. Turgut, D. Zusin, D. Legut, K. Carva, R. Knut, J. M. Shaw, C. Chen, Z. Tao, H. T. Nembach, T. J. Silva, S. Mathias, M. Aeschlimann, P. M. Oppeneer, H. C. Kapteyn, M. M. Murnane, and P. Grychtol, Phys. Rev. B 94, 220408(R) (2016).
- [56] M. Hofherr, S. Häuser, J. K. Dewhurst, P. Tengdin, S. Sakshath, H. T. Nembach, S. T. Weber, J. M. Shaw, T. J. Silva, H. C. Kapteyn, M. Cinchetti, B. Rethfeld, M. M. Murnane, D. Steil, B. Stadtmüller, S. Sharma, M. Aeschlimann, and S. Mathias, Sci. Adv. 6, eaay8717 (2020).